Lipid Bilayer Vesicle Fusion: Intermediates Captured by High-Speed Microfluorescence Spectroscopy

Guohua Lei and Robert C. MacDonald
Department of Biochemistry, Molecular Biology and Cell Biology, Northwestern University, Evanston, Illinois

ABSTRACT The fusion of lipid bilayers can be visualized under the fluorescence microscope, but the process is very fast and requires special techniques for its study. It is reported here that vesicle fusion is susceptible to analysis by microspectrofluorometry and that for the first time, the entire fusion process has been captured. In the case of giant (>10-μm diameter) bilayer vesicles having a high density of opposite charge, fusion proceeds through stages of adhesion, flattening, hemifusion, elimination of the intervening septum, and uptake of excess membrane to generate a spherical product very rapidly. These investigations became possible with a fluorescence microscope that was modified for recording of images simultaneously with the collection of fluorescence emission spectra from many (>100) positions along the fusion axis. Positively-charged vesicles, composed of *O*-ethylphosphatidylcholine and dioleoylphosphatidylcholine, were labeled with a carbocyanine fluorophore. Negatively-charged vesicles, composed of dioleoylphosphatidylglycerol and dioleoylphosphatidylcholine, were labeled with a rhodamine fluorophore that is a resonance energy transfer acceptor from the carbocyanine fluorophore. An electrophoretic chamber allowed selection of pairs of vesicles to be brought into contact and examined. Spectral changes along the axis of fusion were captured at high speed (a few ms/frame) by operating a sensitive digital camera in the virtual-chip mode, a software/hardware procedure that permits rapid readout of selected regions of interest and by pixel binning along the spectral direction. Simultaneously, color images were collected at video rates (30 frame/s). Comparison of the spectra and images revealed that vesicle fusion typically passes through a hemifusion stage and that the time from vesicle contact to fusion is <10 ms. Fluorescence spectra are well suited to rapid collection in the virtual-chip mode because spectra (in contrast to images) are accurately characterized with a relatively small number of points and interfering signals can be removed by judicious choice of barrier filters. The system should be especially well-suited to phenomena exhibiting rapid fluorescence change along an axis; under optimal conditions, it is possible to obtain sets of spectra (wavelength range of ~150 nm) at >100 positions along a line at rates >1000 frames/s with a spectral resolution of ~10 nm and spatial resolution at the limit of the light microscope (~0.2 μm).

INTRODUCTION

Membrane fusion, although critical to cellular function, is a complex process, and model systems consisting of lipid bilayers in the form of vesicles or planar membranes have been popular subjects for the study of elementary fusion processes. Most such investigations have involved the assay of interactions of populations of vesicles in cuvette fluorometers (Malinin et al., 2001; Meers et al., 2000; Hoekstra and Düzgünes, 1993; Stamatatos et al., 1988; Kendall and MacDonald, 1982; Struck et al., 1981), although individual vesicles have been investigated by video fluorescence microscopy (Garcia et al., 2001; Pantazatos and MacDonald, 1999; Korlach et al., 1999; Niles and Cohen, 1987; Niles et al., 1996; Rand et al., 1985; Ohki, 1993). Because vesicle fusion is very rapid relative to video image collecting time (33 ms), details of the process are inaccessible with this approach and a faster recording method is needed. Of relevance to this report, one manufacturer (Princeton Instruments) has recently developed a digital camera and controlling software that allow data collection of binned subarrays at speeds well over 1000 frames per second (fps).

Color charge-coupled device (CCD) cameras, of both the one- and three-chip types, that are commonly used in fluorescence microscopy of nonstatic objects, conventionally use color filters or liquid crystals and are restricted to collection of fixed wavelengths of light. This limitation can be a particular problem when analyzing multilabeled fluorescent samples. In some applications, i.e., fluorescence resonance energy transfer (FRET) (Meer et al., 1994; Lakowicz, 1999), color cameras cannot distinguish the acceptor from donor fluorescence intensity when two wavelengths are close. For these and other studies, intensities at specific fluorophores wavelengths are needed.

The alternative approach is to split the light path with a prism and record the image through separate filters (Niles et al., 1996). The disadvantages of such an approach include the difficulty of matching and synchronizing the images, loss of intensity, and, moreover, sampling only a portion of the total emission spectrum. Some of these drawbacks are avoided by using a dichroic filter to split the image (Optical Insights, Santa Fe, New Mexico), but spectral information remains very limited.

Mounting a scanning spectrometer with a photomultiplier (PMT) detector on a microscope allows our acquiring full wavelength changes of fluorescence, but this arrangement lacks spatial resolution and cannot view rapidly-occurring

Submitted August 29, 2002, and accepted for publication March 28, 2003.
Address reprint requests to Robert C. MacDonald, Dept. of Biochemistry, Molecular Biology and Cell Biology, Northwestern University, Evanston, IL 60208. Tel.: 847-491-5062; Fax: 847-467-1380; E-mail: macd@northwestern.edu.

0006-3495/03/09/1585/15 $2.00

events (Tsien and Bacskai, 1995). Furthermore, these instruments have limitations in some biological applications—for example, fluorescence energy resonance transfer assessment of molecular interactions, or multilabeled samples in which fluorescent probes spectra overlap (so it is difficult to separate out each spectrum with multiple emission filters alone; see Haralampus-Grynaviski et al., 2000; Schultz et al., 2001).

Recent spectral imaging developments include a highly sensitive spectrograph for use in scanning fluorescence microscopy for FRET. High sensitivity was achieved with a prism in combination with a back-illuminated CCD camera and a $(160 \text{ pixel})^2$ image was recorded in 1.5 min at 3 ms dwell time per image pixel with a spectral resolution of ~5 nm at 550 nm (Frederix et al., 2001). Rouse and Gmitro designed a laser point scanning system capable of reading 256 frames of data in 4.1 s to produce a three-dimensional data set (256^2 spatial by 26 spectral) with a spatial resolution of 3 mm and a spectral resolution of 10 nm (Rouse and Gmitro, 2000). Eng and collaborators obtained spectra and images of myocytes at video rates using a modified fluorescence microscope (Eng et al., 1989). Ford and collaborators (Ford et al., 2001) developed a computed tomography imaging spectrometer capable of simultaneously acquiring full spectral information (450–750 nm) from every position element within its field of view (75×75 μm^2) with spatial and spectral sampling intervals of 1.0 μm and 10 nm, respectively. This powerful instrument is neither capable of high-speed operation nor commercially available.

In this article, we describe a microscope based on standard commercial components that can very rapidly obtain full fluorescence spectra from multiple points along a one-dimension spatial array. Simultaneous two-dimensional color images can be recorded at video rates and temporally keyed to the spectra. This instrument was capable of capturing spectral changes of donor-acceptor fluorophore pairs during fusion of oppositely-charged lipid vesicles. It provided the highest precision of spatial and temporal data on membrane fusion of any system to date.

MATERIALS AND METHODS

Chemicals

1,2-dioleoyl-*sn*-glycero-3-ethylphosphocholine (EDOPC) was prepared as previously described (Rosenzweig et al., 2000). Our synthesis generates the trifluoromethane sulfonate salt; the chloride salt is available from Avanti Polar Lipids (Alabaster, AL). 1,2-dioleoyl-*sn*-glycero-3-phosphoglycerol (DOPG), 1,2-dioleoyl-*sn*-glycero-3-phosphocholine (DOPC), and 1,2-dioleoyl-*sn*-glycero-3-phosphoethanolamine-*n*-[lissamine-rhodamine-B-sulfonyl] (Rh-PE) were also from Avanti. 3,3′-dioctadecyloxacarbocyanine perchlorate (DiO) was from Molecular Probes (Eugene, OR). 3-aminopropyltrimethoxysilane was from Aldrich Chemical (Milwaukee, WI).

Instruments

The spectra were recorded with an I-PentaMAX camera, an intensified digital camera that can be operated at high frame rates with special control software (Princeton Instruments, Trenton, NJ). An analog color video camera (SHC-710NA, Samsung Opto Electrics, Secaucus, NJ) was used to collect color images. A spectrometer with a 150 grooves/mm grating (SpectraPro-150, Acton Research, Acton, MA) of the imaging type was used to project spectrally dispersed light from the object onto the CCD surface of the I-PentaMAX. Winspec32 software (Roper Scientific, Trenton, NJ) was used for control of the spectrometer and collection of spectra. A PC-to-TV converter (Ultimate 2000, Dobbs-Stanford, Stanford, CA) allowed transformation of the digital signal to an analog signal and hence to record the spectral frame sequences and time information by VCR. Timing of the spectral frame and vesicle image was done with the shareware program MiniTimer (www.csdn.net; BMD Technology, Beijing).

Preparation of giant unilamellar vesicles (GUVs)

The procedure for preparation of negatively-charged giant vesicles was similar to that described previously (Pantazatos and MacDonald, 1999). The vesicle composition for studying weak adhesion was DOPG (12 μg), DOPC (180 μg), and Rh-PE (8 μg). That for studying stable hemifusion was DOPG (40 μg), DOPC (152 μg), and Rh-PE (8 μg). The vesicle composition for studying full fusion was DOPG (100 μg), DOPC (92 μg), and Rh-PE (8 μg). In all cases, the lipids were mixed in chloroform in a small vial. Then the solvent was removed with a stream of argon and the residue was placed under high vacuum for 1 h. The dried mixture was hydrated in a 0.5 ml, 320 mM sucrose solution. A characteristic cloudiness was observed after several hours of incubation at room temperature, which indicated that the vesicles were ready to use, although typically they were left overnight.

Positively-charged giant vesicles for simple adhesion studies contained EDOPC (12 μg), DOPC (152 μg), and DiO (8 μg). EDOPC is a derivative of DOPC prepared by forming the ethyl ester of the unsubstituted phosphate oxygen (MacDonald et al., 1999). Vesicles for stable hemifusion study were composed of EDOPC (40 μg), DOPC (152 μg), and DiO (8 μg). Vesicles for studying vesicle full fusion were prepared from EDOPC (100 μg), DOPC (92 μg), and DiO (8 μg). These lipids were mixed in chloroform and treated as described above for negative vesicles except for the following difference: after overnight hydration, the vesicle suspension was put in the freezer at −20°C for ~2 h or until completely frozen. The vial was kept at room temperature for one day without stirring, at which time the vesicle suspension was ready to use.

The choice of the probes for the two types of vesicles was dictated by the need for a positive dye for the positive vesicles and a negative dye for the negative vesicles so that the probe would not behave differently from the bulk lipids because of electrostatic reasons. DiO, the positive dye, and RhPE, the negative dye, are both are quite photostable and rather economical, but other reasons for their choice had to do with practicalities of the microscope-based experiment, namely that to choose the GUVs to bring together, one must be able to simultaneously see and distinguish them. These two dyes can both be excited with a broadband excitation filter of the type sometimes used with fluorescein, which is not only convenient, but has the added advantage that when the lipids of the two vesicles mix, there is efficient energy transfer; both strong sensitized emission from rhodamine and strong quenching of the carbocyanine occur. This is useful in analyzing images, and not absolutely necessary in spectroscopy (unless one wants to establish donor-acceptor distances), but it does mean that the signal change is more dramatic than it would be without energy transfer. The dyes were used at approximately the concentration of maximum brightness; higher concentrations were less bright because of excessive self-quenching. An important consideration was that higher concentrations mitigated photobleaching. Some additional issues having to do with probes are dealt with in the section on the microscope, below.

Electrophoresis control chamber

Vesicles were manipulated electrophoretically by imposing an electric field along the axis of one of two orthogonal channels in a chamber mounted on

the stage of the microscope. The chamber was based on an earlier design (Pantazatos and MacDonald, 1999). A large microcoverslip (60 mm × 48 mm, 0.17-mm thick) and a smaller coverslip were attached to each other, face-to-face, with four squares of double-stick tape, so as to form two intersecting microchannels, as shown in Fig. 1. The width of each channel was ~3 mm and the thickness ~0.15 mm.

Because of the negative charges on the surface of glass, positively-charged vesicles adhere to and eventually rupture on the surfaces of untreated coverslips. To reduce such adhesion, we treated the coverslip surface of one channel with 3-aminopropyltrimethoxysilane so as to confer a weak positive charge upon the glass surface. Briefly, the coverslip was cleaned in an ultrasonic bath with 1% SDS for 30 min, rinsed in deionized water, then immersed in concentrated sulphuric acid for 20 min, rinsed in deionized water 5×, and dried in an oven at 110°C. After cooling to room temperature, the coverslip surface of the cross channel area was immersed in 3-aminopropyltrimethoxysilane (0.05% w/v in ethanol) for 10 min to make it almost neutral and the positively-charged vesicle channel area was immersed for 30 min. The coverslip was rinsed several times with ethanol, and then placed in an oven at 110°C. Platinum or stainless steel wire electrodes were fixed near the outer ends of each of the channels and opposite pairs of electrodes were separately connected to two variable DC power supplies capable of generating up to ~25 V with on-off-on toggle switches for reversing polarity.

The volume between the slide and coverslip was filled with a solution consisting of 320 mM sucrose and glucose (see next paragraph). A 5-ml portion of positive vesicle suspension was introduced into the end of the positively-coated channel and a like-volume of the negative vesicles into the other channel. Using a 1-ml pipette, a small volume of solution was gently sucked out from the end of one of the cross channels to bring the two suspensions together at the junction in the center of the chamber. This step is taken only just before the beginning of an experiment to assure there is a fresh boundary between the two vesicle populations. Because large vesicles electrophoresce faster than smaller vesicles, one can identify pairs of large, pristine vesicles in each of their suspensions and bring them together without interference by manipulating the direction of the electric field across the channel intersection. In addition to allowing selection of large vesicles that are most suitable for detailed observation, this electrophoretic manipulation of vesicles also means that the background is quite low because the smaller vesicles are left behind.

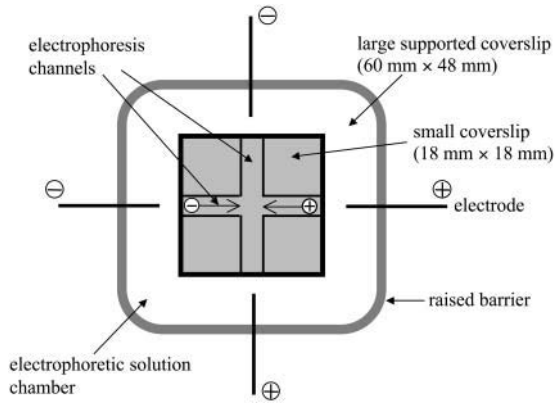

FIGURE 1 Top view of electrophoretic chamber for vesicle control. The chamber is filled with ~3 ml solution, then vesicle suspensions are added to the opposite ends of a channel. A small volume of solution (~1 ml) is sucked out from one end of the perpendicular channel to bring the residual vesicles together at the intersection in the center. Suitable oppositely-charged vesicles are brought to contact by controlling the polarity of the two sets of electrodes; one polarity is shown, but a switch allows reversal of polarity of each pair of electrodes independently.

Procedure for ensuring that vesicles are at the same vertical position

The electrophoretic manipulation system is extremely simple and effective for moving vesicles in the plane of field of the microscope, that is, from front to back (vertical axis) and from right to left (horizontal axis) as viewed through the microscope. It does not, however, provide for moving vesicles normal (z-axis, or optical axis) to that plane. In the absence of a method to manipulate vesicles along the z-axis, considerable time is lost in seeking vesicles that have the same z-coordinate and will, in fact, contact when brought to the same horizontal and vertical coordinates. To avoid this inconvenience, we suspended vesicles in a solution with a density very slightly lower than that of their internal aqueous compartment. All vesicles thus settled to the bottom of the chamber and were hence necessarily in the same plane and could be manipulated into contact without concern for the z-coordinate. The osmolarities of the two solutions were the same to avoid vesicle volume changes. The low density, external phase solution consisted of a 3:1 (by volume) mixture of 320 mM sucrose (density: 1.0423 g/ml) and 320 mM glucose (density: 1.0234 g/ml) so that the solution density was 1.0376 g/ml. The internal solution of the vesicles was 320 mM sucrose, which is 0.45% denser than the external solution. Under these conditions, heavy vesicles sink slowly (a few min) to the lower surface of the chamber and may be manipulated electrophoretically as desired. We avoided a large difference between inside and outside so that the downward force was small; this eliminated rough landings that can lead to rupture as well as adhesion, which would preclude manipulating vesicles horizontally. The settled vesicles can remain in contact with the glass surface treated as described in the previous section for ~1 h without problems from adhesion or rupture.

Spectrum and image system

A schematic diagram of the component organization is shown in Fig. 2. The instrument consisted of the following major components: 1), an inverted fluorescence microscope; 2), a multiport optical coupler to attach two viewing devices to the same output port of the microscope; 3), an imaging spectrometer (here ''imaging'' refers to the fact that the exit side of the spectrometer is designed to display the spectrum at an exit plane rather than on an exit slit, as is the case of most monochromators found in cuvette-based fluorometers); 4), a video color camera which fed into a video recorder; 5), an intensified digital camera capable of high-speed operation under special conditions, connected to a computer for camera control and recording of the spectra; and 6), signal manipulation instrumentation for digital-to-analog signal conversion (D-A converter) and for combining video images (quad-processor). All components in this system are commercially available.

The fluorescence microscope

The experiments were conducted with a Nikon Diaphot TMD inverted epifluorescence microscope (Nikon USA, Melville, NY) equipped with a plan Neofluor 100× objective lens ($NA = 1.3$) and a 100-watt mercury lamp. Neutral density filters were used to control light intensity and reduce photobleaching during observation of vesicles. One of our most important applications involved fluorescence resonance energy transfer, and to both observe donor and acceptor fluorescence through the microscope as well as to obtain their spectra, we used the following epifluorescence filter components; a 450/490-nm bandpass exciter filter; a 510-nm dichroic beam splitter; and a 520-nm longpass barrier filter. These filters were quite satisfactory in studies using DiO as donor and Rh-PE as acceptor. Because the acceptor fluorescence increases after energy transfer conditions are established (fusion or hemifusion), the rhodamine-labeled vesicles are initially considerably less bright than the DiO-labeled vesicles, but the situation reverses when extensive energy transfer occurs, and the green DiO intensity falls while the red Rh-PE intensity increases.

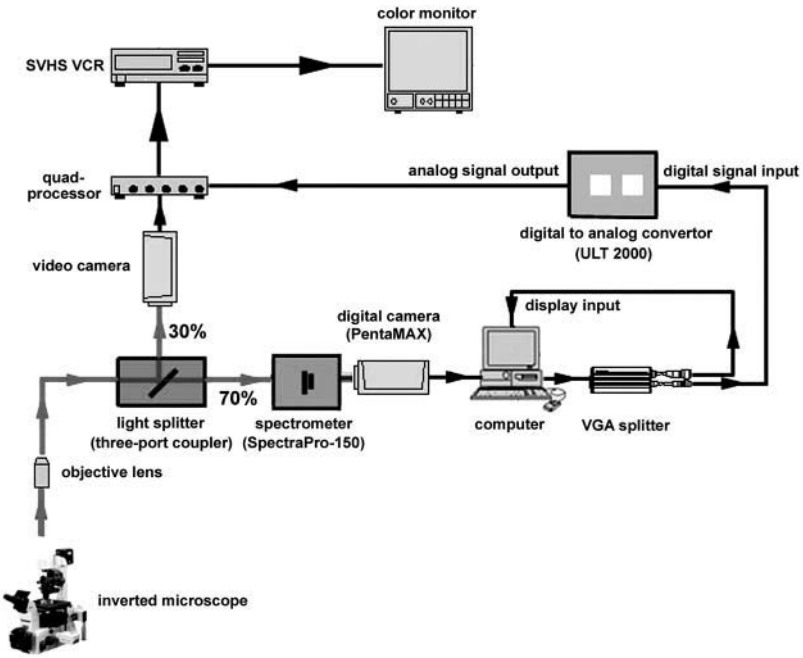

FIGURE 2 Schematic diagram of the spectrometer and imaging system.

Collection of images simultaneously with fluorescence spectra

Because it is useful to have images of the objects from which spectra are being collected, we divided the fluorescence light such that the image of the vesicles was directed through the side port of a multiport coupler and then through a 0.5× magnification relay lens (Optem, Fairport, NY; which also provided for par-focus with the eyepieces) and the light through the straight-through port was directed to the spectrometer. The split was 30% for the image and 70% for the spectra. The beam splitter in the coupler deflected light to the video camera at right angles and simultaneously introduced a large amount of polarization. Since the light from the vesicles was also polarized, in this case radially due to the orientation of the acyl groups, the result was that the sides of vesicles were much brighter that the top and bottom (as viewed). This problem was eliminated without reduction of light intensity by introducing a quartz/silica wedge depolarizer (Halbo Optics, Chelmsford, UK) in front of the relay lens.

Video image processing

Qualitative changes in fluorescent probe density, distribution and diffusion on vesicles were recorded with a color video camera. A color camera (Samsung SHC-710NA) that can achieve high sensitivity by on-chip integration was used (1–128 images can be summed). The basic frame collection time of this camera is 1/60 s, and one can combine two or more continuous frames into one frame (each output frame is the average of two or more frames). This process is good for obtaining high quality color video images, but at rates that were necessarily lower than video rates. Typically, we used a shutter setting of 2 to detect weak fluorescence (in particular for rhodamine-labeled vesicles) so that the real time of each frame would be 1/30 s, i.e., normal video rate. A color video recorder (Super VHS ET; JVC Americas, Wayne, NJ) was used to record images at a resolution of 608 × 406 pixels (30 Hz). Video images were digitized with a Studio DC10 (Pinnacle Systems, Mountain View, CA) video capture card at the same resolution as that of the VCR.

Photobleaching was reduced during preparatory steps (selecting and moving vesicles close to one another) with a 25% neutral density filter in the excitation light path. With full illumination, DiO intensity was reduced by 40% in 10 s, whereas Rh-PE intensity diminished only 10%. With the neutral density filter in place, the losses of intensity for DiO and Rh-PE were only 12% and 5%, respectively, over 10 s.

Time stamps were written on each video frame with the MiniTimer program to synchronize color images with the spectra, which were automatically numbered in sequence by the digital camera used to capture spectra. Since the frame repetition rate was known for the spectral camera, the two sets of images could be put into temporal correspondence.

Spectrometer

The Acton spectrometer was fitted with a grating with 150 grooves/mm, the lowest dispersion available, to limit the wave lengths collected to just the emission spectra of DiO and Rh-PE. The entrance slit width of this instrument is manually adjustable from <10–3000 μm with a micrometer. A 100-μm slit width corresponds to a projection of 1 μm onto the object when a 100× objective lens is used. The slit width determines the width of the strip in the object from which spectra are obtained. A wider slit corresponds to a wider swath across the object, and it also means a larger amount of light is collected. A narrow slit defines a smaller region in the object for spectral collection, but the narrower the slit, the less light collected. The relationship among the slit, the region in the object being examined, and the dispersion of the light from that object are illustrated in Fig. 3.

High-speed data collection with a digital camera in the virtual-chip mode

To accelerate data collection, the I-PentaMAX digital camera provides a very high-speed subregion mode called virtual-chip operation. In this mode, the user masks the CCD chip to illuminate only a subregion of the chip; this region (but not regions below it) is rapidly shifted under the frame transfer mask and digitized by custom programming of the CCD, with the result that continuous data collection is possible at rates from 50 to 1000 fps, or even higher with binning.

The I-PentaMAX camera allows hardware binning at the same time as data collection (as opposed to software postprocessing). Although the bin size can be set independently in the *x*- and *y*-directions, there is little speed

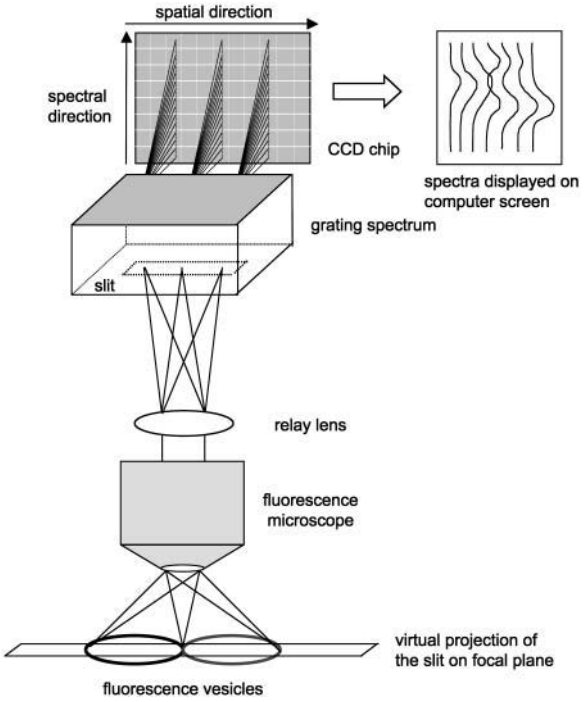

FIGURE 3 Illustration of the relationship between the region in the object being examined and the dispersion of the light from it by a spectrometer grating. The light (fluorescence) from vesicles is collected by the fluorescence microscope and passes through the entrance slit of the spectrometer. The light is dispersed into its spectral components by the grating, and then projected onto the CCD chip. From the chip, the signal is transferred to computer where the spectra are displayed and stored. It should be noted that the light is collected from a region in the object defined by the projection of the slit onto the object. Hence, spectra are obtained from segments along the slit projection corresponding to columns of pixels in the *y*-direction, normal to the axis of the slit. For simplicity, only a few spectra are shown. In fact, for the camera described here, 512 spectra may be obtained simultaneously.

advantage to binning in the *x*-direction and doing so reduces spatial resolution, so we binned only in the *y*-direction (spectral direction). This provides a great speed and a sensitivity advantage because a known spectrum can be established with high precision with rather few points. For example, with 512 pixels in the *x*-direction and 170 pixels in the *y*-direction (170 pixels is the maximum in virtual-chip mode), the data transfer time was 19.3 ms per frame and our measured signal-to-noise ratio (*S/N*) was 33, whereas with 10:1 binning in the *y*-direction, the time was reduced to 2.94 ms and the *S/N* increased to 53. For 90 pixels with 9:1 binning in the *y*-direction and 100 pixels without binning in the *x*-direction, we could collect data at 1060 fps.

Chip masking with a bandpass filter

The charges from the virtual chip are shifted under the frame transfer mask at the same time a new region from below is shifted into the area of the virtual chip. It is hence essential that no significant charges be already present on the pixels below the region of interest. This is assured by masking in the optical path so that light does not fall on the region below the virtual chip. Masking can be achieved by applying a mechanical or optical mask or by positioning a bright image at the RIO against a dark background on the remainder of array. In our case, because we were using fluorescence, provided that no vesicles were imaged onto the chip other than those of interest, physical masking was not required (a fortunate circumstance, since adjusting and changing physical masks is time-consuming). Stray light did, however create some problems in that the long wavelength ends of the spectra were artificially shifted to higher intensities. This was eliminated with a shortpass filter (SP650) to cut off wavelengths longer than those desired, namely, 650 nm. The I-PentaMAX camera is sufficiently insensitive to short wavelengths (<400 nm), that filtering out light at wavelengths shorter than those of interest were not necessary. It was, of course, necessary to center the spectrum so that it coincided with the virtual-chip area chosen.

RESULTS

Signal optimization

The optical paths of the imaging spectrometer and fluorescence microscope are shown in Fig. 3. The net effect of the optics is to collect light from a narrow rectangular strip through the object and then to disperse that light into its component wavelengths by diffraction from the grating in the direction perpendicular to the axis of strip. This spectrally-dispersed light then impinges on the photosensitive surface of the detector, which in this case is the chip of the I-PentaMAX camera (the process is analogous to that of an array detector spectrophotometer except that our instrument also obtains spatial information). The *y*-direction on the chip records intensity as a function of wavelength. The *x*-direction corresponds to distance along the strip. In a microscope-based imaging spectrometer, an important function of the slit is to define the width of the region of interest in the object from which the spectra are collected. This, in turn, may also influence the amount of light collected from the object. Normally, the slit of a spectrophotometer determines spectral resolution, hence we characterized the relation between signal-to-noise ratio and frame rate, slit width, etc.

The cooled (−20°C) I-PentaMAX camera exhibits both low noise and low background. Without cooling, the noise level was ~30 units (arbitrary), while the background (no sample on microscope stage) was 400 units at an intensifier gain of 70% with a subregion 170 (10:1 binning) × 512 pixels and a frame rate of 340 fps. With cooling, the noise level was reduced to 10 units and the background to ~50 units. The background noise is thus small compared to the background signal, which presumably comes predominantly from stray light in the incident epifluorescence portion of the microscope.

A DiO-labeled vesicle was used to assess signal and noise levels under practical conditions. Fig. 4 *A* shows the spectrum at a single position (1 pixel column at the CCD chip) on the spatial axis. With a region of interest of 90 pixels in the spectral direction and with 9:1 binning, the frame rate was 1060 fps. The labeled numbers in the figure are the value of standard deviation at each measured wavelength from the formula: $STD_\lambda = [1/(n-1)\sum_{i=1}^{n}(y_i(\lambda) - \bar{y}(\lambda))]^{1/2}$, where $\bar{y}(\lambda)$ was the fit function data value at wavelength λ (The fit function $\bar{y}(\lambda)$ was obtained with all measured data by polynomial regression fitting), $y_i(\lambda)$ was the original

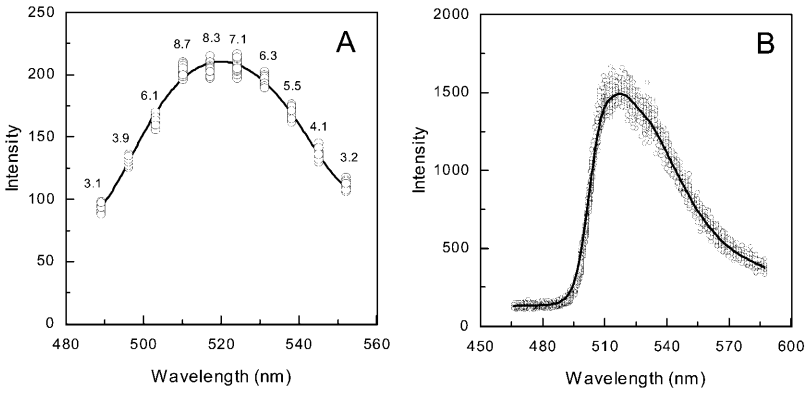

FIGURE 4 The spectrum of a DiO-labeled vesicle at a single position (1 pixel at the CCD chip, corresponding to 0.15 mm in the image plane) along the spatial direction and its fitted curve. (*A*) 90 pixels in the spectral dimension were used with 9:1 binning and the frame rate was 1060 fps. The labeled numbers on the curve are standard deviations (from 30 frames). The spectrometer entrance slit width was 20 μm, corresponding to 0.2 μm in the image plane. The spectrum shown is one of 10 spectra, each from a single region with nominal dimensions of 15 μm $\times$ 15 μm on the CCD chip. The camera gain setting was 80%. (*B*) 160 pixels in spectral direction with a rate of 195 fps. The spectrometer entrance slit width was 100 μm, corresponding to 1 μm in the image plane. The camera gain setting was 80%.

intensity at wavelength λ, and n was the number of measured points. We take the standard deviation of signal (STD_λ) as the noise and $\bar{y}(\lambda)$ as the signal. The signal-to-noise ratio was calculated according to formula: $S/N = STD_\lambda/\bar{y}(\lambda)$. It was found that $S/N = 25$ at 518 nm in Fig. 4 *A*. Comparing Fig. 4, *A* and *B*, it is evident that, for long exposure time, the signal-to-noise ratio is higher than for a short exposure time. Such behavior is expected for digital cameras.

Under our conditions involving the spectrometer coupled to a microscope with a high-power objective lens, even at the widest practical slits, the spectral resolution is more than adequate for our purposes. For 90 pixels with 9:1 binning, the spectral resolution was ~9 nm. Thus, the slit width effectively only controls the area of the object examined (which in many cases will also influence the intensity of light gathered from the object). A large slit width increases the spectral signal intensity, but reduces resolution in the *y*-direction, perpendicular to the slit (that is, it increases the width of the strip through the object from which light is collected). Although in some applications, including ours, a wide slit can be desirable both because of increased intensity and a larger sampling of the object of interest, in many cases it would be preferable to be able to obtain spectra from as narrow as strip as can be resolved by the light microscope. We therefore determined the relationship between slit width and signal intensity. Fig. 5 shows the full relationship between slit width and *S/N* ratio. We choose a 1-mm fluorescent polystyrene microsphere as a test sample, and with neutral density filters, adjusted its fluorescence intensity to be approximately the same as that of a DiO-labeled vesicle. The break at ~100 mm is due to the fact that, at this point, the slit was as wide as the diameter of the microsphere; up to that point increasing the slit width increased the fluorescence area from the microsphere. When the slit width was larger than the microsphere diameter, the slope of the relationship between fluorescence and slit width became almost flat, because increasing the slit only leads to increased background/stray light.

The digital camera scanning area is directly related to frame rate. The smaller the scanning area, the shorter the time. Also, shorter exposure times decrease the *S/N* ratio. Fig. 6 shows the effect of the virtual-chip scanning area and of the corresponding frame rate on the *S/N* ratio. The virtual scanning area was changed only in the *y*-(spectral) direction. The scanning areas were 160 $\times$ 100, 150 $\times$ 100, 140 $\times$ 100, ...10 $\times$ 100 pixels without pixel binning. As may be seen, a high frame rate reduced *S/N*; i.e., at 50 fps, S/N = 116, whereas at 680 fps, $S/N = 43$.

Spectrofluorometric characterization of a bilayer vesicle

To characterize the application of this instrument to lipid vesicle fusion, we initially carried out a series of experiments on a single vesicle. The slit width was 100 μm and the digital camera gain was 70%. Fig. 7 *A* is the fluorescence image of a vesicle labeled with DiO. The gray bar in the middle of the image represents the virtual projection of spectrometer slit onto the vesicle. Note that centering the slit on the vesicle is necessary to obtain sharp spectra. If the slit were not in the

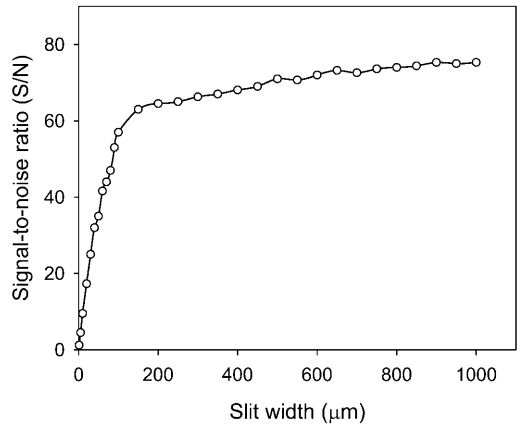

FIGURE 5 Effect of the entrance slit width of the spectrometer on the *S/N* ratio taken at peak of the spectral band. A 1.0-μm fluorescent microsphere was used as the object. The camera gain setting was 70%. The virtual-chip area was 100 (spatial direction) $\times$ 160 (spectral direction) pixels and 10:1 binning was done in the spectral direction. The frame rate was 650 fps. The change in slope at ~100 μm on the curve corresponds to the point where the projection of the slit width became equal to the diameter of the microsphere.

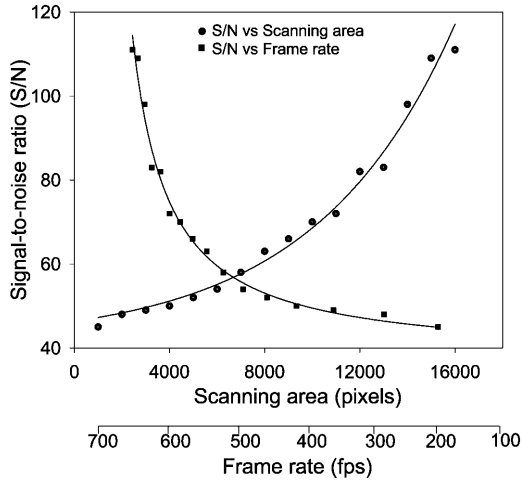

FIGURE 6 Effect of the virtual-chip scanning area or frame rate on the *S/N* ratio. The virtual scanning area was changed by increasing the number of pixels of the region of interest in the *y*-direction, and the dimension in the *x*-direction was held constant. The scanning areas were 160 × 100, 150 × 100, 140 × 100, ... 10 × 100 pixels. The scanning time or frame rates corresponding to scanning area were also recorded, and are shown on the lower horizontal axis.

center of the vesicle, the border of vesicle membrane would not be perpendicular to the slit direction, and would affect the sharpness of spectrum in the position corresponding to vesicle membrane border. Fig. 7 *B* depicts the spectral distribution along the slit with ''distance'' corresponding to the position along the projection of slit. The two peaks at 15 and 33 μm correspond to the edges of the vesicle. Fig. 7 *C* shows the fluorescence intensity along the slit direction at 510 nm, i.e., it corresponds to a slice through Fig. 7 *B* perpendicular to the wavelength at 510 nm. Fig. 7 *D* shows a fluorescence spectrum at single position on the distance axis; i.e., it corresponds to a 1.0-μm-wide slice through Fig. 7 *B* perpendicular to the distance axis at distance = 33 μm.

Weakly charged vesicles interact, but barely

In Figs. 8 and 9 are presented images and spectra, respectively, of vesicles in which 10% (charged lipid + charged fluorophore) of the total lipids had a net charge. These vesicles contact one another and remain weakly adherent, but nothing else happens. The region of contact is yellow according to the images (Fig. 8) and there is no detectable energy transfer according to the spectra (Fig. 9). There was no significant flattening and the contact region remained small. The spectra did not detectably change so diffusion of dye between vesicles was negligible.

Fluorescence images and emission spectra along the axis of hemifusion

When the fraction of charged lipid in vesicles is increased, they begin to exhibit interactions that change the bilayers dramatically. Fig. 10 shows vesicles with 24% charge lipids obtained at video rates, i.e., 33 ms/frame. Initially, the positive, DiO-labeled vesicle florescence was very bright, whereas the negative, rhodamine-labeled vesicle was considerably less bright (because of its longer wavelength absorption peak, it is rather inefficiently excited). As the vesicles come into contact, the contact area becomes yellow, corresponding to simultaneous emission of both red and green from the same area. Thereafter there are dramatic color and intensity changes (see Fig. 10, *E–J*) which we interpret as due to hemifusion; the color of the contact area changes

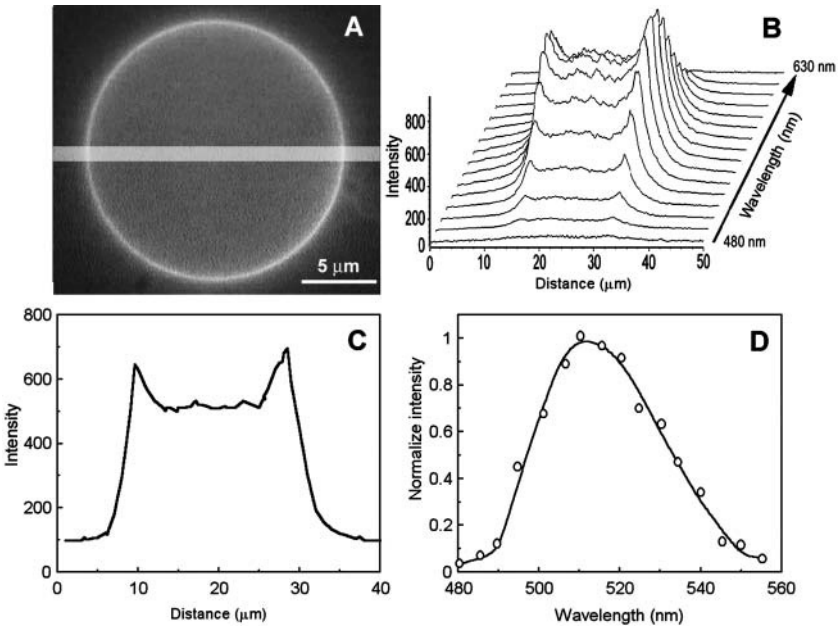

FIGURE 7 A single vesicle fluorescence image and spectra. (*A*) The fluorescence image of a vesicle labeled with DiO. The gray bar in the middle of the image represents the virtual projection of the spectrometer slit (it is 1.0-μm wide) on the vesicle. (*B*) The vesicle spectral distribution along spectral entrance slit direction. This is one of the DiO spectra acquired along the length of the gray rectangle as shown in *A*. There were 320 pixels (~50 μm, so a spectrum was nominally collected every 50/320 = 0.16 μm) in spatial direction, 160 pixels with 10:1 binning in the spectral direction, and the frame rate was 470 fps. (*C*) Fluorescence intensity profile of the vesicle along the slit direction. (*D*) DiO fluorescence spectrum obtained from *B*. The circles are the original data from *B* at position of 33 μm; the line is the fitted curve.

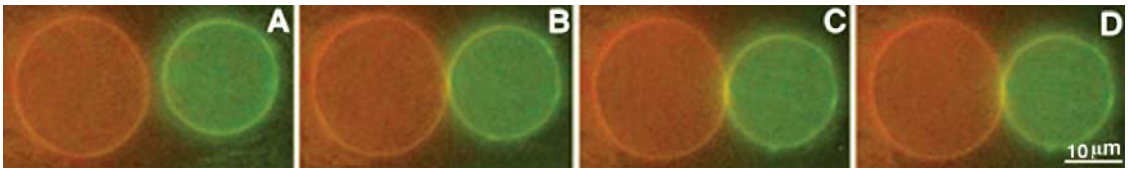

FIGURE 8 Video images of contact and weak adhesion, without further interaction, of two vesicles with low surface charge density (10% of full charge). (*A*) Time course before contact. (*B*) Time course at vesicle contact (0 ms). The color changed to yellow in the contact zone, suggesting overlap of red and green emission and probably not very much energy transfer, although quantitation is problematic. (*C*) A small increase in adhesion is indicated by the increase of area that became yellow (66 ms). (*D*) The vesicles are very slightly more adherent, although the yellow color intensity has not increased significantly (132 ms).

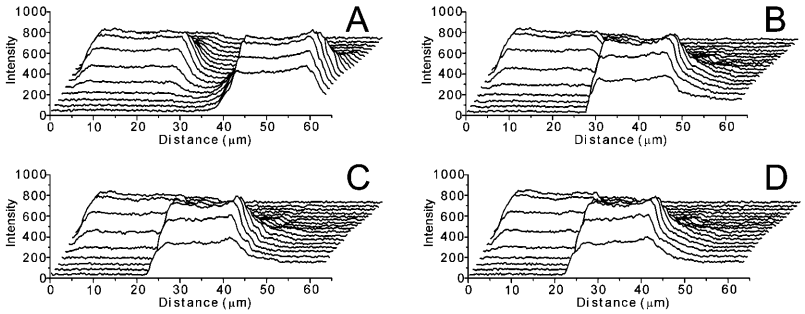

FIGURE 9 Time course of spectral change during two contacts of the two vesicles shown in Fig. 8. (*A*) Time course of spectra before vesicle contact. (*B*) Time course of spectra at vesicle contact (0 ms). (*C* and *D*) Spectra at 65 and at 130 ms. The spectral range is from 500 to 650 nm (from front to back). Slit width was 200 μm. The lack of spectral change reveals that there is essentially no energy transfer across the contact region, despite the fact that these vesicles are adherent, albeit weakly.

from yellow to red, the contact area becomes slightly flatter, and then red color can be seen beginning to diffuse from the contact area over the surface of the positive vesicle, reducing the intensity of the green color in the process. The negative vesicle becomes brighter red as interdiffusion brings DiO into the negative vesicle. Both the increase in red intensity and reduction in green intensity are due to energy transfer; as the two probes intermix, the rhodamine fluorescence becomes sensitized and the DiO fluorescence becomes quenched. Color diffusion from green to red over the vesicle membrane is apparent within 660 ms. Finally, the entire vesicle became red, as shown in Fig. 10 *J*. The spectra for this same interaction, obtained every 5 ms, or ~6× faster than the images, reveal energy transfer shortly after contact (Fig. 11, *B* and *C*). This is initially most evident from the sharp increase in the longer wavelength rhodamine (560 nm) emission. Within 5 ms after contact, the rhodamine-labeled vesicle peak intensity increased from 1000 to 2500 units. By 10 ms, it had increased further, and then subsequently gradually dropped (Fig. 11 *E*). Very much later, at 385 ms, it was considerably lower (Fig. 11 *F*) as the fluorophore became distributed uniformly over both vesicles. As indicated above, the increase in rhodamine emission and decrease in DiO emission are due to increased energy transfer, largely due to mixing of the two dyes as hemifusion leads to intermixing of the lipids of the outer monolayer of the two vesicles. Some contribution to an increased intensity may also come from the increased contact zone area (see Fig. 11, *C* and *D*). The spectra in Fig. 11 were obtained with a slit width of 200 mm, which means that fluorescence was collected from a 2-μm-wide strip through the center of the two vesicles.

Fluorescence images and emission spectra along the axis of fusion

Fig. 12 shows video images of full fusion of two vesicles. These vesicles contained 54% net-charged lipids. They came into contact and fused to form a spherical product in less than one video frame (33 ms), even though these were rather large vesicles (>25 μm). The rapidity of the process relative to video recording rates clearly precludes identifying any intermediates. However, by simultaneously recording spectra (Fig. 13), which can be done at much higher rates, intermediate stages can clearly be identified. An increase in rhodamine emission is already visible in Fig. 13 *B*, where, judging from the distance dependence of the intensity, the vesicles have just barely come into contact. Full contact appears at Fig. 13 *C*; between Fig. 13, *C* and *D*, there is a very sharp increase of rhodamine emission and some quenching of DiO emission at the contact zone. Whereas close contact of the two vesicles surface would, in itself, be expected to produce some energy transfer, it would not extend significantly beyond the contact zone, whereas, in fact, rhodamine fluorescence in Fig. 13 *C* can be seen to have become extended into the cationic vesicle. We interpret this as a consequence of hemifusion whereby membrane mixing leads not only to much increased energy transfer at contact but also into the cationic vesicle. (It is recognized that additional work will be required to establish standard curves from which one can extract distance information before this intermediate state can be understood in terms of precisely what changes bilayers are undergoing.) Within an additional 5 ms at most, between Fig. 13, *D* and *E*, the two vesicles have completely fused since the smaller negative vesicle

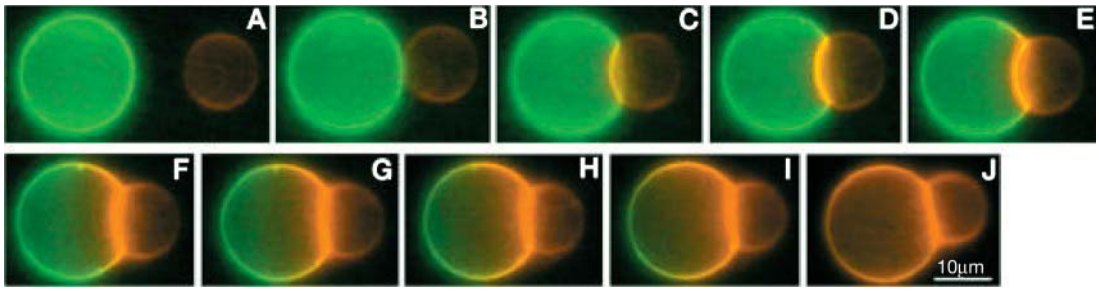

FIGURE 10 Hemifusion video images. Vesicles had moderate net charges (24%). Time sequence of the images: (*A*) Before the vesicles contacted. (*B*) Two vesicles contact (at 0 ms). (*C*) Contact zone formed (at 33 ms). (*D*) Stable contact (at 66 ms). (*E*) Contact area color changed from yellow to red (at 99 ms). At the same time, red fluorescence appeared on the green vesicle, showing that Rh-PE diffused from the negatively- to the positively-charged vesicle. (*F–I*) Images at 132, 165, 231, and 330 ms after contact. (*J*) At 660 ms after contact; the green color was significantly quenched and the red color increased along the vesicle contact area. Hemifusion as a stable final state is commonly seen with vesicles having an intermediate content of charged lipid.

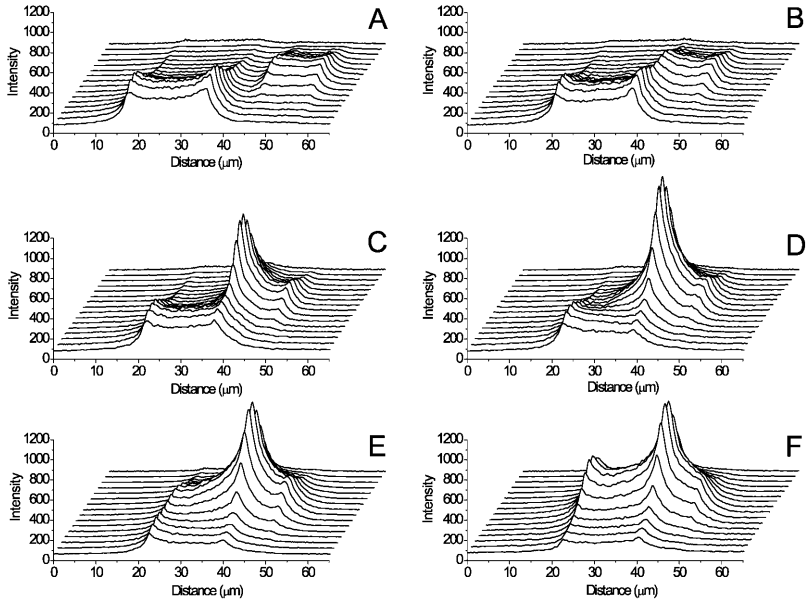

FIGURE 11 Spectral change with time during vesicle hemifusion. The video images are shown in Fig. 10. (*A*) Time course of spectra before two vesicles contacted. (*B*) Time course of spectra at 0 ms (time of contact). (*C–F*) Spectra at 5, 10, 15, and 385 ms after vesicle contact. The spectral range is from ~500 to 650 nm (from front to back). Slit width was 200 μm.

(rhodamine-labeled) has disappeared and the rhodamine emission is now found on the left side of the fused product vesicle. The whole time for fusion is thus well under 10 ms. In Fig. 13, *F* and *G*, the rhodamine fluorescence increases again, as it interdiffuses into DiO on the surface of the fused vesicle. By Fig. 13 *H*, ~1 s after fusion, rhodamine has spread to the far side of the fused vesicle and the probes are evidently near equilibrium, for the rhodamine intensity increased much on the far side of the vesicle (*right*).

DISCUSSION

Microscopy and spectroscopy

As described above, although images of fusion can be obtained moderately rapidly with a color video camera, because of the way the data are handled, a spectrometer allows spectra along the axis of fusion to be obtained at much higher rates. Fusion of oppositely-charged lipid bilayer vesicles is a rapid process; consequently we combined these two information collection modes in a microspectrometer which permits the acquisition of spatial and spectral information at a high rate and images simultaneously but at a slower rate. Although the extremes of performance have not been completely tested, it is clear that this system is capable of revealing spectral changes in the contact zone between vesicles at a high enough rate to permit the eventual complete documentation of what happens to fluorescent probes during membrane fusion.

The spatial resolution of each spectrum is ultimately determined by the resolution of the optical system. With 512 pixels in each dimension of the CCD chip, the I-PentaMAX camera covers a field ~80 mm wide when coupled with a 100× objective lens. The resolution of the digital camera is hence formally 80/512, or ~0.16 μm/pixel in the *x*-direction, or spatial direction (parallel to the slit projection), but this is more apparent than real, for the microscope objective optical resolution is only 0.21 μm, at best. Because of the camera

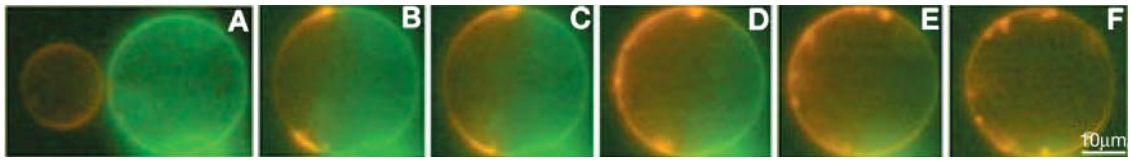

FIGURE 12 Video images of full fusion. Vesicles contained a high proportion of lipids with a net charge (54%). (*A*) Time sequence before two vesicles contacted (at 0 ms). (*B*) Time sequence at full fusion (at 33 ms). (*C–F*) Images at 99, 330, 660, and 6600 ms. Fluorescent probes have diffused along the membranes. Some small pink particles appeared on the inside of the fused vesicles; these regions are probably invaginations and represent the area that became excess when the two vesicles fused at constant volume.

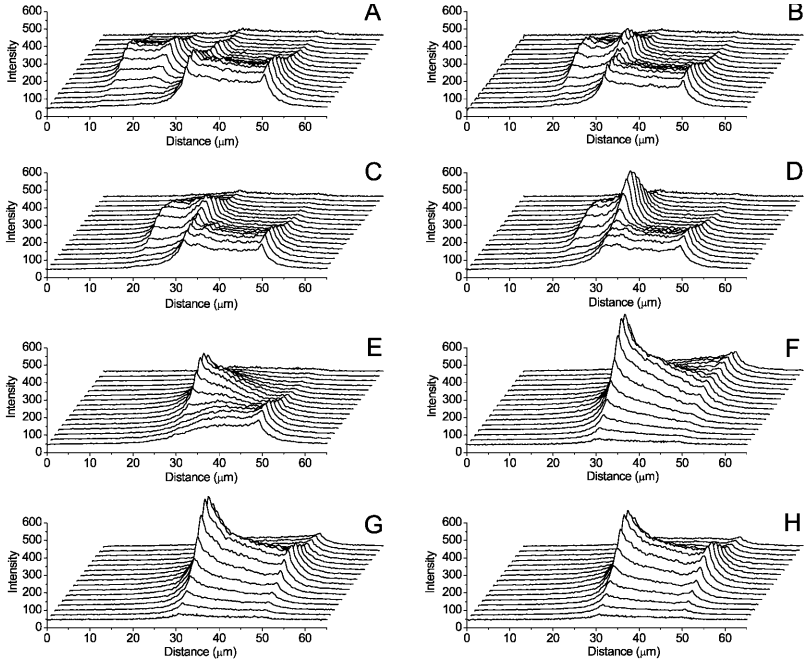

FIGURE 13 Time course of spectral change during vesicle fusion. The video images are shown in Fig. 12. (*A*) Time sequence of spectra before the vesicles contacted. (*B*) Time sequence of vesicles contacted (at 0 ms). (*C–H*) Spectra at 5, 10, 15, 385, 465, and 1025 ms after vesicles contacted. The spectral range is from ~500 to 650 nm (from front to back). Slit width was 200 μm.

design, the width of the region of interest in the *x*-direction has a small effect on readout time, so we usually chose the maximum pixels (512). In the *z*-direction (axial), the resolution *dz* is determined by the objective lens. The full width at half-maximum of the axial irradiance distribution defines the axial resolution, which is given by $dz = 1.4\ nl/(NA)^2$, where *NA* is numerical aperture and *n* is the immersion oil refractive index (Corle et al., 1986; Sheppard and Wilson, 1978). At 550 nm, with $NA = 1.3$ and $n = 1.5$, *dz* is equal to 1.2 μm. The resolution in the Y_{obj} direction (perpendicular to the slit projection on the object) depends on the slit width of the spectrometer and, in practice, useful signals may be obtained at slit widths that correspond the *y*-axis distance as small as the limit of optical resolution. The XY_{obj} plane spatial resolution in conjunction with *dz* defines a diffraction-limited volume, which responds to the three-dimensional resolution of the microscope. Therefore, in theory, the spectrum in a given position is formally from a volume of $0.21 \times 0.21 \times 1.2\ \mu m^3$ in our experiments.

The spectral resolution also depends on slit width, the number of grooves on the optical grating, and the resolution of the detector used to collect the images. For the purpose of determining energy transfer between organic fluorophores with broad emission peaks, it is adequate to define the change of the spectrum as a whole, and, in such cases, high resolution is not an issue. We were therefore able to exploit the virtual-chip mode of the I-PentaxMAX camera, which however, limits the maximum number of pixels in the *y*- or spectral direction to 170 (each pixel is 15 mm × 15 mm). For a region of interest of such a dimension, with a 150-grooves/mm grating, the spectral resolution is 1 nm. Since this is still very small compared to the half-widths of the bands of the fluorescent probes we dealt with, which were of the order of 50 nm, we could raise the data collection speed as well as increase the signal-to-noise ratio by using binning techniques, e.g., binning 10 pixels into a super pixel. In general, the spectral resolution at a specific wavelength can be calculated by multiplying the number of binned pixels by the bandwidth per pixel at that wavelength. However, the projection of the light from the grating on the CCD chip depends on wavelength. Therefore, the spectral resolution for a CCD chip changes slightly with wavelength. In our

experiments there were typically 10–17 super pixels in the spectral direction, so that the effective spectral resolution was between ~9 and 15 nm. This could, of course, be increased by using a grating with a higher line density or a camera with smaller pixels. However, in the case of organic molecular spectra with which we are concerned, there is little value in higher spectral resolution. As is evident from Fig. 4, seven or 10 points define the DiO spectrum (particularly when the shape is already known accurately) essentially as precisely as a much larger number of points, so that, for broad spectra, noise is a much more relevant issue than is spectral resolution per se.

The maximum temporal resolution is governed by the collecting area of the camera. For our experiments, 1000 fps or higher can be obtained at acceptable *S*/*N* and spectral resolution. As indicated, pixel binning was used, since it increases both data collection rate and *S*/*N*. This approach would be even more useful for weak fluorescence probes.

Giant vesicles and their manipulation

The ability to prepare giant vesicles is clearly essential for the study of fusion by light microscopy. It is relatively easy to produce negatively-charged or neutral giant vesicles in sucrose solution using gentle hydration (Reeves and Dowben, 1969; Needham et al., 1988). For producing positively-charged giant vesicles, this method is less satisfactory. A number of articles have described alternative methods (Akashi et al., 1996; Menger and Angelova, 1998; Angelova and Dimitrov, 1986; Angelova et al., 1992). Our modification of the slow hydration procedure involved inclusion of a freeze-thaw step, a very simple change that greatly increased the percentage of GUVs. This procedure is not only suitable for EDOPC but also the cationic amphiphile, DOTAP. The procedure was even more satisfactory with the neutral DOPC and, in fact, inclusion of DOPC in cationic formulations generally improved the GUV yield. On the other hand, freezing and thawing negatively-charged vesicle preparations was actually counterproductive and led to smaller vesicles. Such an outcome may, however, depend upon environmental conditions, for, in our experience, freezing and thawing the same lipids can lead to either increases or decreases in vesicle size, depending upon the environment (Oku and MacDonald, 1983; MacDonald et al., 1994).

This study has focused on vesicles in nonelectrolytes because of ease of preparation. Giant vesicles can also be prepared in physiological ionic strength solutions, but the yield is lower. Somewhat surprisingly, interaction outcomes are not greatly different at high and low ionic strength, at least for the vesicle compositions described here. Similarly modest differences were also represented previously for both individual interactions (Pantazatos and MacDonald, 1999) and population interactions (Pantazatos et al., 2003).

In the examination of vesicle fusion, control of vesicle movement is important. To avoid significant fluorescence photobleaching, large-diameter, unilamellar vesicles need to be located and moved into position without undue delay. The electrophoretic cell we described allows such control. It has the further advantages of being easy to use and very inexpensive.

Hemifusion can be a stable state when charge densities are moderate; it is predicted to be a very short-lived intermediate during complete fusion

Figs. 8–13 indicate that, at very low surface charge density, oppositely-charged vesicles interact very weakly, highly charged vesicles fuse completely, and vesicles with intermediate charge density may proceed only to the hemifusion stage. Although limited, this pattern conforms to what was observed previously in a much larger survey, but only at video speeds (Pantazatos and MacDonald, 1999). At low charge density (Figs. 8 and 9), there is weak adhesion, but negligible flattening. Clearly there is little change in these membranes, suggesting that in the absence of adhesion forces significant to distort membranes, little will change. With increased charge density, hemifusion of vesicles becomes common and when the neutral lipid is PC, the hemifusion is a rather slow process. Vesicles can remain in contact for 10s or more ms and then, quite suddenly, the fluorophore begins to migrate across the contact zone. Until the abrupt onset of dye transfer, there is only observable energy transfer at the contact zone, indicating that the two surfaces may remain in contact without fluorophore transfer, but that a stochastic event occurs to initiate transfer. Frequently, there is a small change in the contact angle at the junction of the two vesicles that is simultaneous with the onset of dye transfer. We interpret the transfer of dye as the onset of hemifusion and that the contact angle change is due to the weakening of the septum under the influence of the bilayer tensions (see next section). Proof that these events constitute the signature for the onset of hemifusion will require additional investigation, but presently, the hypothesis appears quite reasonable.

When the charge density in the vesicle membranes is high (half or more of the lipid is charged), then the transition from contact to full fusion is very rapid. Despite its speed, we can identify transfer of fluorophore between vesicles before there is any detectable change in positions of the vesicles (Fig. 13). Although vesicle positions can be identified in the spectral mode of data collection, contact angles at the contact zone cannot, so only the initiation of dye transfer is available to identify stages in this rapid process. We believe that such dye transfer signifies hemifusion in this situation as well, but additional data collection at exposure times of a ms or less will be needed to establish whether it is also abrupt on the timescale of full fusion. This is an extrapolation from our observations at lower charge density; however, there are substantive reasons for suspecting that hemifused intermedi-

ates will exist during rapid full fusion. These reasons come from an analysis of the operative forces, as discussed in the next section.

Why fusion intermediates may be short-lived: forces affecting the interaction of oppositely-charged vesicles

As we have seen, fusion can be very fast—the processes of adhesion, hemifusion, and full fusion can be over in milliseconds. It was the rapidity of this process that led to the need for new instrumentation. Having described that instrumentation and the results obtained with it, it is appropriate to next consider the reasons why fusion intermediates may have such short lifetimes. Such an analysis requires that we first recognize the forces that operate when the vesicles come into contact. With respect to anionic vesicles adhering through the mediation of multivalent cations, these were addressed by Parsegian, Evans, and Rand (Evans and Parsegian, 1983; Parsegian and Rand, 1983). Kozlov and Markin (1984), in a article that, unfortunately, was not readily available in the United States, presented a detailed analysis of what they described as the ''adhesion-condensation'' mechanism of fusion. MacDonald (1988) independently proposed a related mechanism, but without detailed energetic analysis. Both of these proposals were originally intended to explain the fusion of phosphatidylserine vesicles by calcium ion. There are significant differences in the two mechanisms, but both depended on the recognition that calcium ions neutralize the anionic charge of phosphatidylserine, creating a tendency for the headgroups of the external monolayer of the participating vesicles to condense into a smaller area per molecule. A tension thus arises in the external monolayers and this can be relieved at the contact zone where the monolayers can rend because the resulting fissures can be filled in by the tails of the inner monolayer, with the result that one or more hemifused regions form at the contact zone between the two vesicles. In an early article that supported a role for external monolayer tension, Ohki found a good correlation between ions that raise the surface tension of an anionic lipid monolayer and fusion of bilayer vesicles of the same lipids; indeed, he proposed that increased hydrophobicity due to cation binding is what leads to fusion (Ohki, 1982). Kozlov and Markin suggested that the headgroups of the outer monolayers interdigitated, and they analyzed the energy costs of forming gaps under such conditions. MacDonald assumed that the oil-oil contacts of hemifusion would reduce the costs of gap formation to negligible values and focused on the fact that the tension generated in the vesicles by their adhesion/flattening would pull apart the weakened septum, causing full fusion. Because electrostatic interactions from headgroups of one monolayer to the headgroups of another can also lead to headgroup condensation, when fusion of oppositely-charged vesicles was discovered, we recognized that the MacDonald mechanism could be readily modified to be applicable to this fusion situation (Pantazatos and MacDonald, 1999). The Kozlov and Markin mechanism could also be adapted to oppositely-charged vesicles, but, in any case, because their term, ''adhesion-condensation,'' is apt for the mechanism that we propose, it is used here. Some aspects of the adhesion-condensation hypothesis, e.g., hemifusion, have counterparts in hypotheses for fusion of natural membranes (and some model systems); Zimmerberg and Chernomordik (1999) have expertly reviewed the involvement of lipids in several such systems.

In the case of vesicles that have 50% or more charged lipid, the remainder being PC, fusion occurs in about one-half of the encounters, with most of the remainder leading to rupture of one or both of the vesicles (Lei and MacDonald, unpublished; Pantazatos and MacDonald, 1999). By ordinary video fluorescence microscopy, no intermediates could be seen. Nevertheless, the process of fusion can be presumed to proceed through events dictated by the physical forces that must operate. These forces are related to those alluded to in the previous paragraph, and although some of the presumed intermediates have been discussed previously (Pantazatos and MacDonald, 1999), a detailed description of the presumptive forces has not been given and it is hence appropriate to do so here. Diagrams of the presumed steps are provided in Fig. 14. In Fig. 14, *1*, the vesicles have just contacted, but the adhesion forces (the downward vector indicates the force that the lower vesicle exerts on the upper vesicle) have not yet deformed the vesicles. In Fig. 14, *2*, adhesion leads to flattening of the vesicles against one another. As the tension (*diagonal vector*; for simplicity, shown in the drawing only for the upper vesicle) increases due to the vesicle flattening, the vertical (upward) component grows larger and begins to oppose the adhesion force. Simultaneously, the horizontal component increases its pull outward on the diaphragm composed of the planar portions of adherent bilayers in the contact zone. In Fig. 14, *3*, this process has come to equilibrium, that is, the mutual adhesion of the two vesicles has generated a tension, the vertical component of which is just equal to the adhesion force due to the other vesicle. This situation thus corresponds to the maximum tension that can be produced in the vesicle bilayers due to the adhesion force. Note that although the horizontal component of the vesicle bilayer tension increases as the area of the contact increases, the former is the *result*, not the *cause* of the latter; adhesion is the primary phenomenon and as the adherent area grows, the flattening of the vesicles increases the tension on their bilayers. Furthermore, it should be emphasized that the tensions shown in Fig. 14, *2* and *3*, represent the vectors that are tangent to the bilayers at the circumference of the contact zone. Elsewhere, the tension is isotropic, but at the circumference of the contact zone it is not and, at that locus, only the component of the total tension in the plane of the contact zone is relevant to fusion.

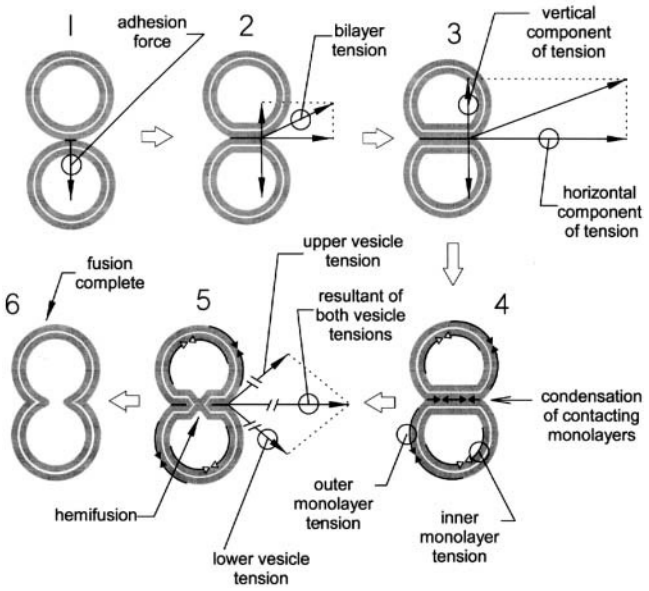

FIGURE 14 Processes and tensions involved in contact fusion of oppositely-charged vesicles. The figure shows the progression of events that may be presumed to occur between contact and full fusion of two oppositely-charged vesicles. The thick, gray lines represent monolayers; each circle consists of two such lines, hence is a single bilayer vesicle. *1*. Vesicles contact. *2*. Vesicles adhere and begin to flatten. Vectors show components of tension acting at edge of contact surface. *3*. The tension in the vesicle bilayers has come into equilibrium with the adhesion force. *4*. During flattening, the two surfaces neutralize each other, reducing repulsion within each monolayer and inducing a tendency to condense to a smaller area/molecule. (*Curved arrows* on monolayer surfaces are a reminder that the bilayer tension operates over the whole surface, although there may be a transient differential tension between inner and outer monolayers as the contact zone monolayer condenses.) *5*. External monolayers rend within the contact zone; the inner monolayers fill the gaps so-created. *6*. The residual tension in both vesicles now acts on a single bilayer that spans the gap in the hemifusion region and if it exceeds the lysis tension of that bilayer, full fusion ensues.

As the vesicles flatten against one another, the bilayer tensions increase as shown in Fig. 14, *2* and *3*; however, simultaneously, another process operates to affect the two participating surfaces. For simplicity, this process, which comes from the mutual neutralization of one charged surface by the other, will be described as if it occurred not simultaneously, but subsequently to, the mutual flattening of the two vesicles. Because each of the vesicles is composed of lipids either entirely or mostly of the same ionic charge, the headgroups within each vesicle repel one another. This causes all monolayers of the component bilayers to be more expanded than otherwise. (This effect has been quantified in monolayers at the air/water interface; at 40 mN/m, the average area of negative and positive monolayers is ~5% larger than the area of a PC monolayer or than the area of a neutral monolayer of equimolar cationic and anionic lipids; MacDonald, Gorbonos, Momsen, and Brockman, in preparation.) Upon contact, monolayers at the contact zone will largely neutralize each other, reducing repulsion within each monolayer and creating an additional tension at the contacting monolayers, but one that does not affect the inner monolayers (*arrows* in the contact zone in Fig. 14, *4*). This tendency to condensation might be expected to recruit lipid from the water-facing portion of the external monolayers; however, such a process is effectively precluded by the hydrophobic force, which resists separation of headgroups facing water. In contrast, there is little resistance to condensation of headgroups in the contacting surfaces because the gaps that would be created can be filled by the hydrophobic tails of the inner monolayers coming together (Fig. 14, *5*). This is, in fact, hemifusion, and because this kind of gap formation in the contact zone can lead to oil-oil contacts, it would only be weakly resisted by a line tension at the edges of the gaps.

Once the openings in the outer monolayers appear and hemifusion begins, the bilayer tensions, which remain in effect because of continuing vesicle adhesion, act, not on two bilayers in the contact zone, but now on a single bilayer. If the adhesion energy is sufficient, the resultant tensions will exceed the lysis tension of the bilayer and break the septum, leading to full fusion, as seen in Fig. 14, *6*. Full understanding of the process of fusion in this system requires knowing exactly what is going on when the gaps form in the outer monolayers to initiate hemifusion. Our suggestion is that hemifusion fills the gaps, but there are other possibilities. Inverted micelles, such as proposed by Hui et al. (1981) and Verkleij (1984), would also be consistent with a condensation of headgroup area; however, the energy costs would probably be too large to fill in the whole area of the gaps with inverted micelles. (Based on our monolayer experiments, ~5% of the total contact area would be involved.) A version of interdigitation of the headgroups of the oppositely-charged contacting monolayers such as in the original Kozlov-Markin hypothesis might also be considered. In any case, whatever happens when the two contacting monolayers neutralize each other, the essential point is that both of those monolayers will acquire some form of defect that weakens it so that the tension that has built up in the two flattened vesicles becomes concentrated on that defect. Hemifusion, per se, would not seem absolutely necessary, for the septum could be pulled apart by vesicle tension as soon as a defect arises that is significant enough to destabilize it. Our evidence, nevertheless, implicates a defect that, if not actually a hemifused intermediate, at least allows lipid exchange before full fusion. It is relevant that, recently, Chanturiya et al. have re-examined the Ca-PS system with the objective of distinguishing among three hypotheses for fusion, and obtained rather definitive evidence in support of the critical role in hemifusion of the differential surface tension across the vesicle bilayer (Chanturiya et al., 2000). This publication has a figure that corresponds to portions of our Fig. 14 except that vesicle flattening and its consequences are omitted; however, a later article considered increased

internal pressure leading to full fusion (Chanturiya et al., 2002).

How much tension can be expected from the flattening of two vesicles against one another? When a vesicle flattens onto a planar surface, the volume that was originally in the section above that plane is pushed into the rest of the vesicle. The volume of that section is given by solid geometry as $\pi h^2(3r\text{-}h)/3$, where r is the vesicle radius and h is the height of the section (the amount of flattening). From the well-known formulas for sphere volume and area, one can calculate the amount of stretching that vesicle flattening through adhesion would impose on the vesicle membrane. For example, for $h = 0.3$ and $h = 0.5$ (values that cover the range we commonly observe), the vesicle membrane must stretch by ~3.3 and 6.3%, respectively. The critical area strain—the fractional increase in area needed to rupture a bilayer—is ~3% for phospholipid bilayers (corresponding to a lysis tension of ~5 mN/m; Needham and Nunn, 1990). The stretch that is produced by adhesion is hence in the range that will rend bilayers, much less a half of a bilayer (which is relevant after hemifusion occurs).

It should be noted that, if the charge density on the vesicles is too low, there may be insufficient tension in the vesicles to induce full fusion. Furthermore, if the charge density is high, the tension developed by adhesion may be large enough to rupture the vesicle in regions outside of the contact zone. Hence, we generally find more rupture at high charge density and more hemifusion at moderate charge density. Finally, we would point out that kinetic effects can operate to bias the outcomes of vesicle interactions. As noted above, the rise in bilayer tension in the vesicles and the condensation of headgroups at the contact zone, while both dependent on vesicle-vesicle adhesions, could have slightly different time dependencies, which could influence the final product. Similarly, when hemifusion occurs the septum is weakened, but also, hemifusion opens a path for exchange of the charged lipids to the opposite vesicle. Such lipid exchange will reduce the net charge density and hence also adhesion which, in turn, also reduces the tension in the vesicles. Thus, if full fusion does not occur very shortly after hemifusion is initiated (or at least defects in the outer monolayers form), then full fusion is likely to be abrogated and the vesicles will remain in the hemifused state.

CONCLUSIONS

A variety of biophysical methods can be used to obtain structural, dynamic, or orientation information on populations of lipid vesicles, but these methods generally lack the capability to meaningfully decipher spatial and temporal details of molecular interactions in the case of heterogeneous vesicles, which is the typical situation. The microfluorometric imaging approach can, in conjunction with FRET techniques, provide unambiguous and detailed information on kinetics, specificity, heterogeneity, and conformational dependence of lipids in bilayers on an ~1–8 nm scale. This approach demonstrates that it is possible to capture of stages of fusion of vesicles that, by standard video fluorescence microscopy, would be impossible. The approach is not only highly suited for the study of bilayer fusion, but it should also be very useful for other fast membrane and cellular processes that exhibit major change along a single axis and especially when there is a possibility of small spectral shifts due to environmental effects during interaction. The microfluorometric approach revealed that fusion intermediates are indeed short-lived, but given the modes of action of the known forces in fusion of oppositely-charged bilayer vesicles, this is readily rationalized.

We thank Ruby MacDonald, Spiro Pantazatos, and Dennis Pantazatos for help in the laboratory in many ways.

This research was supported primarily by National Institutes of Health grant GM 57305, but also partially by GM 52329.

REFERENCES

Akashi, K., H. Miyata, H. Itoh, and K. Kinosita, Jr. 1996. Preparation of giant liposomes in physiological conditions and their characterization under an optical microscope. *Biophys. J.* 71:3242–3250.

Angelova, M. I., and D. S. Dimitrov. 1986. Liposome electroformation. *Faraday Discuss. Chem. Soc.* 81:303–311.

Angelova, M. I., S. Soleau, P. Meleard, J. F. Faucon, and P. Bothorel. 1992. Preparation of giant vesicles by external AC electric fields. Kinetics and applications. *Prog. Coll. Polym.* 89:127–131.

Chanturiya, A., P. Scaria, O. Kuksenok, and M. C. Woodle. 2002. Probing the mechanism of fusion in a two-dimensional computer simulation. *Biophys. J.* 82:3072–3080.

Chanturiya, A., P. Scaria, and M. C. Woodle. 2000. The role of membrane lateral tension in calcium-induced membrane fusion. *J. Membr. Biol.* 176:67–75.

Corle, T. R., C.-H. Chou, and G. S. Kino. 1986. Depth response of confocal optical microscopes. *Opt. Lett.* 11:770–772.

Evans, E. A., and V. A. Parsegian. 1983. Energetics of membrane deformation and adhesion in cell and vesicle aggregation. *Ann. N. Y. Acad. Sci.* 416:13–33.

Eng, J., R. M. Lynch, and R. S. Balaban. 1989. Nicotinamide adenine dinucleotide fluorescence spectroscopy and image of isolated cardiac myocytes. *Biophys. J.* 55:621–630.

Ford, B. K., C. E. Volin, S. M. Murphy, R. M. Lynch, and M. R. Descour. 2001. Computed tomography-based spectral imaging for fluorescence microscopy. *Biophys. J.* 80:986–993.

Frederix, P. L. T. M., M. A. H. Asselbergs, W. G. J. H. M. van Sark, D. J. van den Heeuvel, W. Hamelink, E. L. de Beer, and H. C. Gerritsen. 2001. High sensitivity spectrograph for use in fluorescence microscopy. *Appl. Spectrosc.* 55:1005–1012.

Garcia, R. A., S. P. Pantazatos, D. P. Pantazatos, and R. C. MacDonald. 2001. Cholesterol stabilizes hemifused phospholipid bilayer vesicles. *Biochim. Biophys. Acta.* 1511:264–270.

Haralampus-Grynaviski, N. M., M. J. Stimson, and J. D. Simon. 2000. Design and applications of rapid-scan spectrally resolved fluorescence microscopy. *Appl. Spectrosc.* 54:1727–1733.

Hoekstra, D., and N. Düzgünes. 1993. Lipid mixing assays to determine fusion in liposome systems. *Methods Enzymol.* 220:15–32.

Hui, S. W., T. P. Stewart, L. T. Boni, and P. L. Yeagle. 1981. Membrane fusion through point defects in bilayers. *Science.* 212:921–923.

Kendall, D. A., and R. C. MacDonald. 1982. A fluorescence assay to monitor vesicle fusion and lysis. *J. Biol. Chem.* 257:13892–13895.

Korlach, J., P. Schwille, W. W. Webb, and G. W. Feigenson. 1999. Characterization of lipid bilayer phases by confocal microscope and fluorescence correlation spectroscopy. *Proc. Natl. Acad. Sci. USA.* 96: 8461–8466.

Kozlov, M. M., and V. S. Markin. 1984. On the theory of membrane fusion. The adhesion-condensation mechanism. *Gen. Physiol. Biophys.* 5:379–402.

Lakowicz, J. R. 1999. Principles of Fluorescence Spectroscopy. 2nd Ed., Chap 13–15. Kluwer Academic/Plenum Press. New York.

MacDonald, R. C. 1988. Mechanisms of membrane fusion in acidic lipid-cation systems. *In* Molecular Mechanisms of Membrane Fusion. S. Ohki, D. Doyle, T. D. Flanagan, S. W. Hui, and E. Mayhew, editors. Plenum Press, New York. pp.101–112.

MacDonald, R. C., G. W. Ashley, M. M. Shida, V. A. Rakhmanova, Y. S. Tarahovsky, D. P. Pantazatos, M. T. Kennedy, E. V. Pozharski, K. A. Baker, R. D. Jones, H. S. Rosenzweig, K. L. Choi, R. Qiu, and T. J. McIntosh. 1999. Physical and biological properties of cationic triesters of phosphatidylcholine. *Biophys. J.* 77:2612–2629.

MacDonald, R. C., F. D. Jones, and R. Qiu. 1994. Fragmentation into small vesicles of dioleoylphosphatidylcholine bilayers during freezing and thawing. *Biochim. Biophys. Acta.* 1191:362–370.

Malinin, V. S., M. E. Haque, and B. R. Lentz. 2001. The rate of lipid transfer during fusion depends on the structure of fluorescent lipid probes: a new chain-labeled lipid transfer probe pair. *Biochemistry.* 40:8292–8299.

Meers, P., S. Ali, R. Erukulla, and A. S. Janoff. 2000. Novel inner monolayer fusion assays reveal differential monolayer mixing associated with cation-dependent membrane fusion. *Biochim. Biophys. Acta.* 1467:227–243.

Meer, V. D., B. G. Coker, and S.-Y. S. Chen. 1994. Resonance Energy Transfer: Theory and Data. VCH Publishers, New York.

Menger, F. M., and M. I. Angelova. 1998. Giant vesicles: imitating the cytological processes of cell membranes. *Acc. Chem. Res.* 31:789–797.

Needham, D., T. J. McIntosh, and E. Evans. 1988. Thermomechanical and transition properties of dimyristoylphosphatidylcholine/cholesterol bilayers. *Biochemistry.* 27:4668–4673.

Needham, D., and R. S. Nunn. 1990. Elastic deformation and failure of lipid bilayer membranes containing cholesterol. *Biophys. J.* 58:997–1009.

Niles, W. D., J. R. Silvius, and F. S. Cohen. 1996. Resonance energy transfer imaging of phospholipid vesicle interaction with a planar phospholipid membrane: undulations and attachment sites in the region of calcium-mediated membrane-membrane adhesion. *J. Gen. Physiol.* 107:329–351.

Niles, W. D., and F. S. Cohen. 1987. Video fluorescence microscopy studies of phospholipid vesicle fusion with a planar phospholipid membrane. Nature of membrane-membrane interactions and detection of release of contents. *J. Gen. Physiol.* 90:703–735.

Ohki, S. 1982. A mechanism of divalent ion-induced phosphatidylserine membrane fusion. *Biochim. Biophys. Acta.* 689:1–11.

Ohki, S. 1993. Fusion of spherical membranes. *Methods Enzymol.* 220:79–89.

Oku, N., and R. C. MacDonald. 1983. Differential effects of alkali metal chlorides on formation of giant liposomes by freezing and thawing and dialysis. *Biochemistry.* 22:855–863.

Pantazatos, D. P., and R. C. MacDonald. 1999. Directly observed membrane fusion between oppositely charged phospholipid bilayers. *J. Membr. Biol.* 170:27–38.

Pantazatos, D. P., S. P. Pantazatos, and R. C. MacDonald. 2003. Fusion, hemifusion and rupture of vesicles composed of a cationic phospholipid triester. *J. Membr. Biol.* 194:1–11.

Princeton Instruments. 2000. I-PentaMAX System User Manual. 4411–0062, Ver. 1D.

Rand, R. P., B. Kachar, and T. S. Reese. 1985. Dynamic morphology of calcium-induced interactions between phosphatidylserine vesicles. *Biophys. J.* 47:483–489.

Parsegian, V. A., and R. P. Rand. 1983. Membrane interaction and deformation. *Ann. N. Y. Acad. Sci.* 416:1–12.

Reeves, J. P., and R. M. Dowben. 1969. Formation and properties of thin-walled phospholipid vesicle. *J. Cell. Physiol.* 73:49–60.

Rosenzweig, H. S., V. A. Rakhmanova, T. J. McIntosh, and R. C. MacDonald. 2000. *O*-Alkyl dioleoylphosphatidylcholinium compounds: the effect of varying alkyl chain length on their physical properties and in vitro DNA transfection activity. *Bioconjug. Chem.* 11:306–313.

Rouse, A. R., and A. F. Gmitro. 2000. Multispectral imaging with a confocal microendoscope. *Opt. Lett.* 25:1708–1710.

Schultz, R. A., T. Nielsen, J. R. Zavaleta, R. Ruch, R. Wyatt, and H. R. Garner. 2001. Hyperspectral imaging: a novel approach for microscopic analysis. *Cytometry.* 43:239–247.

Sheppard, C. J. R., and T. Wilson. 1978. Depth of field in the scanning microscope. *Opt. Lett.* 3:115–117.

Struck, D. K., D. Hoekstra, and R. E. Pagano. 1981. Use of resonance energy transfer to monitor membrane fusion. *Biochemistry.* 20:4093–4099.

Stamatatos, L., R. Leventis, M. J. Zuckermann, and J. R. Silvius. 1988. Interactions of cationic lipid vesicles with negatively charged phospholipid vesicles and biological membranes. *Biochemistry.* 27:3917–3925.

Tsien, R. Y., and B. J. Bacskai. 1995. Video-rate confocal microscopy. *In* Handbook of Biological Confocal Microscopy. Plenum Press, New York. pp.459–478.

Verkleij, A. J. 1984. Lipidic intramembranous particles. *Biochim. Biophys. Acta.* 779:43–63.

Zimmerberg, J., and L. V. Chernomordik. 1999. Membrane fusion. *Adv. Drug Deliv. Rev.* 38:197–205.